Journal of Advanced Ceramics
2014, 3(4): 269–277
DOI: 10.1007/s40145-014-0117-x

ISSN 2226-4108
CN 10-1154/TQ

Research Article

Structural, vibrational and magnetic properties of Ti substituted bulk hematite: α-$Fe_{2-x}Ti_xO_3$

Dinesh VARSHNEY[a,*], Arvind YOGI[a,b]

[a]*Materials Science Laboratory, School of Physics, Vigyan Bhawan, Devi Ahilya University, Khandwa Road Campus, Indore 452001, India*
[b]*School of Physics, Indian Institute of Science Education and Research, Thiruvananthapuram 695016, India*

Received: May 10, 2014; Revised: June 20, 2014; Accepted: June 22, 2014

Abstract: Ti doped hematite α-$Fe_{2-x}Ti_xO_3$ ($x=0.0$, 0.0206 and 0.0344) samples are synthesized using solid-state ceramic route technique. Single phase and corundum (Al_2O_3) type structure is revealed from the X-ray diffraction (XRD) pattern. On substitution of Ti at Fe site, all Raman active modes are shifted to higher wave numbers. An additional feature of E_u (LO) mode at about 660 cm^{-1} is observed. The E_u mode frequency is decreased and pronounced systematically as a function of Ti doping, and it reaches a value of 658 cm^{-1} for $x=0.0344$. The coercivity H_c (remanence M_r) for $x=0.0$, 0.0206 and 0.0344 are determined to be 995 Oe (0.44 emu/mg), 1404 Oe (0.00019 emu/mg) and 2023 Oe (0.00016 emu/mg), respectively. The larger coercivity for Ti doped samples can be attributed to their enhanced shape and magneto-crystalline anisotropy. The observed isomer shift (δ) from room temperature Mössbauer data clearly shows the presence of ferric (Fe^{3+}) and Ti^{4+} ions illustrating strong ferromagnetic ordering up to $x=0.0206$ in α-$Fe_{2-x}Ti_xO_3$ hematite and weak ferromagnetic ordering of α-$Fe_{2-x}Ti_xO_3$ for $x=0.0344$.

Keywords: magnetic materials; X-ray diffraction (XRD); Raman spectra; Mössbauer spectroscopy

1 Introduction

The origin of magnetism in hematite α-Fe_2O_3 has long drawn interest as it is the most stable iron oxide under ambient conditions [1]. Hematite α-Fe_2O_3 is commonly described rhombohedral or hexagonal with the space group $R\bar{3}c$ or D_{3d}^6, respectively. The structure of hematite is based on an arrangement of O atoms in a hexagonally close-packing, with Fe^{3+} ions distributed in an ordered fashion in 2/3 of the octahedral sites. The crystal structure is the same as that of corundum Al_2O_3. The framework of hematite is regarded as a set of O and Fe layers, arranged normal to three-fold axis, and the chains of face-sharing octahedra are directed along the c-axis, while Fe^{3+} ions within each chain form pairs separated by an empty interstitial site.

Doping at Fe site in α-Fe_2O_3 influences its electrical, magnetic and other physical properties. The dopants used are usually Ti, Cr, Mn, Co, Ni, Cu, Zn, Al, Ga and Rh. The structural and magnetic properties of parent α-Fe_2O_3 are well established in the recent past; however, an increasing interest of the scientific community in the dopant like Zn ions substituting for Fe^{3+} in the corundum-related structure leads to the formation of cationic and anionic vacancies [2]. The

* Corresponding author.
E-mail: vdinesh33@rediffmail.com

magnetic and structural properties of hematite are also affected by particle size [3], degree of crystallinity [4], pressure [5], doping [2], and mechanical alloying [6] due to its technological applications. Depending upon milling conditions, structural phase transformations of nanostructured hematite to maghemite, magnetite and/or wüstite can be induced.

Raman spectroscopy is a powerful probe for identifying phonon mode, and for hematite α-Fe_2O_3, Raman measurements have been made at normal pressure as well as on applying pressure [7]. The micro Raman spectra of Fe_2O_3 were measured at 62 GPa in a diamond anvil cell and at ambient conditions. The spectra depict all seven phonon (five E_g and two A_{1g}) modes predicted by group theory as $A_{1g}(1)$ (226 cm^{-1}), $E_g(1)$ (245 cm^{-1}), $E_g(2)$ (293 cm^{-1}), $E_g(3)$ (298 cm^{-1}), $E_g(4)$(413 cm^{-1}),$A_{1g}(2)$(500 cm^{-1}),and$E_g(5)$(612 cm^{-1}), respectively [8,9]. Apart from these modes, high-pressure spectra show an additional IR-active E_u mode (~660 cm^{-1}), possibly induced by surface defects or stress. Furthermore, at high pressure an additional Raman mode at 1320 cm^{-1} is observed and is attributed to a second order phonon–photon interaction. Earlier, McCarty has shown strong Raman features in $Fe_{2-x}Cr_xO_3$ at room temperature. The E_u mode (~660 cm^{-1}) of parent hematite varies linearly as a function of Cr doping and it is at about 664 cm^{-1} for $Fe_{1.73}Cr_{0.27}O_3$ and 685 cm^{-1} for $Fe_{0.4}Cr_{1.6}O_3$, respectively [10,11]. McCarty and Boehme [11] observed an additional band when chromium is substituted for iron in α-Fe_2O_3. The band in Raman shift ranges from 664 cm^{-1} for $Fe_{1.73}Cr_{0.27}O_3$ to 685 cm^{-1} for $Fe_{0.4}Cr_{1.6}O_3$, with the shift increasing nearly linearly with increasing chromium content.

The magnetic properties of hematite in bulk form and as spherical nanoparticles have been intensively studied because they have various applications in magnetic storage devices, spin electronics devices, drug delivery, tissue repair engineering and magnetic resonance imaging [3,12–14]. In contrast to spherical nanoparticles, nanorods with their inherent one-dimensional (1D) shape anisotropy may exhibit unique magnetic behavior, which is significantly different from that of the bulk material [15,16]. The magnetic properties of doped hematite are completely altered as compared to that of bulk hematite [17,18].

Mössbauer spectroscopy is an impressive technique to probe magnetic phase as well as to identify magnetic ordering present in the structure. The parent hematite is paramagnetic above the Neel temperature ($T_N \approx 965$ K), it is weakly ferromagnetic at room temperature, and at the Morin temperature ($T_M \approx 265$ K) it undergoes a phase transition to an antiferromagnetic state. The cation (Zn and Ni) substituted (5%) hematite show that T_M is essentially the same for both hematite and similar to that of the undoped one. On the other hand, T_N is lower for Ni doped (5%) hematite ($\approx 883 \pm 2$ K) and Zn doped (5%) hematite ($\approx 874 \pm 3$ K), and both are lower in comparison to T_N for single crystal hematite (965 K) [19]. Although cation substitution suppresses T_N, an increase in T_M for Rh^{3+}, Ru^{3+} and Ir^{4+} is documented [20].

The room temperature Mössbauer spectra for parent hematite α-Fe_2O_3 reveal magnetically resolved lines of hematite and are broaden progressively with increasing milling time (t_m). The static hyperfine field (B_{hf}) decreases from 51.5 T for non-milled sample down to 47 T for the sample with $t_m = 2$ h [21]. As far as cation substitution is concerned, the magnetic cation Cr and non-magnetic cation Ti doped hematite are the most studied ones. The Mössbauer spectra of Cr substituted hematite fitted using only single sextet model at 200 K infer anti-ferromagnetic (AF) ordering; however, weak-ferromagnetic (WF) ordering is noticed at room temperature. On the other hand, the spectra fitted through two-sextet model at about 245 K show the coexistence of both phases (AF and WF). The magnetic hyperfine field (B_{hf}) for Cr substituted Fe_2O_3 at 200 K (AF) is $B_{hf} = 54.45 \pm 0.01$ T and it decreases at 300 K (WF) $B_{hf} = 53.70 \pm 0.01$ T [22].

The near room temperature Mössbauer spectra for $(Fe_{1-x}Ti_x)_2O_3$ ($x < 0.025$) fitted using single sextet of Lorentzian lines confirm the existence of WF phase. On the other hand, below 260 K, two sextets are essential for retracing the Mössbauer spectra consisting of both WF and AF phases. The magnetic hyperfine field (B_{hf}) for Ti doped hematite at 80 K results in $B_{hf} =$ 52.7 T and $B_{hf} = 53.5$ T, while a reduced B_{hf} of about 51.0 T at 295 K with WF phase is documented [23]. On the other hand, non-magnetic cation as Zn substituted hematite prepared by coprecipitation method is less studied, and Zn^{2+} doped hematite documents an additional doublet pattern apart from single sextet and doublet. The hyperfine parameters are affected for Zn^{2+} substitution in hematite, and the decreasing magnetic ordering results in weak ferromagnetic nature as well [24–27]. The structural and spectroscopic properties of doped hematite with

other metal ions have also been investigated earlier [28–30].

The magnetic properties of hematite α-Fe_2O_3 are in general influenced by crystalline nature, average particle size and morphology. The properties of Al substituted hematite, especially magnetic properties, show systematic variations with Al content. Mineralogical and magnetic investigations were carried out on hematite produced by hydrothermal transformation from ferrihydrite and dehydration from goethite. It is observed that hematite produced by hydrothermal transformation display higher saturation magnetization and lower magnetic coercivity than that synthesized using dehydration from goethite [31]. Further, the effect of high hydrostatic pressure on the magnetic remanence of these synthetic Al–hematite has been studied. Half of the initial isothermal remanent magnetization can be destroyed by a pressure of about 1.44 GPa, inferring that hematite is the most pressure sensitive magnetic mineral in single domain state [32].

Hematite α-Fe_2O_3 has attracted much attention as photoelectrode for water oxidation in photoelectrochemical (PEC) systems due to its narrow band gap of 2.1 eV, which is in the visible light region. The Ti doped hematite nanostructures with large surface area were synthesized by the pulsed laser deposition method as photoelectrode for photoelectrochemical cells. It was observed a high photocurrent using the Ti doped hematite nanostructure electrode, which is higher than that of the thin film Ti doped hematite electrode [33]. Earlier, the hematite thin films doped with Ti^{4+} deposited by spray-pyrolysis [34] and on F-doped tin oxide (FTO) substrates by sol–gel method [35] were successfully used in photoelectrochemical splitting of water for solar hydrogen production. It is shown that optimal doping concentration of Ti^{4+} in hematite is 0.02 M, at which photocurrent density and solar to hydrogen conversion efficiency are maximum. Metal oxide as Ti doped hematite photoelectrode has also been used as potential low-cost and electrolyte-stable devices for solar photoelectrochemical hydrogen production [36].

Considering the importance of doped hematite α-Fe_2O_3 as photoelectrode, the hydrostatic effect on magnetic properties and the dimensionality effect, we have prepared Ti^{4+} doped α-$Fe_{2-x}Ti_xO_3$ hematite by solid-state ceramic route technique to investigate the doping effects (tetravalent cation Ti^{4+} for trivalent Fe^{3+}) on the structural, vibrational and magnetic properties following X-ray diffraction (XRD), Raman and Mössbauer spectroscopy. The salient observations on Ti^{4+} doped hematite are: (1) enhanced α-Fe_2O_3 bandwidth due to presence of Ti ions in the lattice due to large anharmonic interactions; (2) coercivity of Ti doped hematite increases as x increases, while remanence decreases as x increases, and larger coercivity for Ti doped hematite is attributed to its enhanced shape and magneto-crystalline anisotropy; and (3) room temperature ^{57}Fe transmission Mössbauer spectroscopy reveals weak magnetic ordering.

2 Experimental techniques

2.1 Synthesis of samples

The polycrystalline samples with the composition α-$Fe_{2-x}Ti_xO_3$ (x = 0.0, 0.0206 and 0.0344) were prepared by the solid-state ceramic route technique as described earlier [24–30]. Stoichiometry amounts for iron oxide (Fe_2O_3) and titanium oxide (TiO_2) were mixed and heated (calcination) at different temperatures (850 ℃, 950 ℃ and 1050 ℃) in air for 24 h. After calcinations, we performed oxygen annealing at temperatures 950 ℃ and 1050 ℃ for 24 h with intermediate grindings. The pellets were finally sintered and annealed at 1050 ℃ in oxygen atmosphere. All the samples were studied on a microscope slide as prepared and their structure was checked by XRD.

2.2 Characterization

2.2.1 X-ray diffraction

The XRD measurements were carried out with Cu Kα radiation using a Rigaku powder diffractometer equipped with a rotating anode scanning (0.01 (°)/step in 2θ) over the angular range 10°–80° at room temperature generating X-ray by 40 kV and 100 mA power settings. Monochromatic X-ray of λ = 1.5406 Å $K_{\alpha1}$ line from a Cu target was made to fall on the prepared samples. The diffraction patterns were obtained by varying the scattering angle 2θ from 10° to 80° in step size of 0.01°.

2.2.2 Raman spectroscopy

The Raman equipment was a Jobin-Yovn Horiba Labram (System HR800) consisting of a single spectrograph (focal length 0.25 m), a holographic grating filter (1800 grooves/mm), and a Peltier-cooled CCD detector (1024 × 256 pixels of 26 μm). The spectra were excited with 632.8 nm radiation (1.95 eV) from a 19 mW air-cooled He–Ne laser (maximum laser power 19 mW) and the laser beam was focused on the sample by a 50× lens to give a spot size of 1 μm; the

resolution was better than 2 cm^{-1}. The laser power was always kept at 5 mW on the sample to avoid sample degradation, except in the laser power dependence experiments. After each spectrum had been recorded, a careful visual inspection was performed using white light illumination on the microscope stage in order to detect any change that could have been caused by the laser.

2.2.3 Magnetization

The magnetization measurements on all the samples under investigation were performed using a vibrating sample magnetometer (VSM). Magnetic measurements for the samples in the powder form were carried out at room temperature using a VSM (Lakeshore 7300 model, USA). The hysteresis curves were obtained for the samples with different compositions. The applied field was varied from 0 to ±10000 Oe, and from the hysteresis curves representing the magnetization process at room temperature (300 K), the saturation magnetization (M_{sat}), remnant magnetization (M_r) and coercive force (H_c) have been determined.

2.2.4 Mössbauer spectroscopy

^{57}Fe transmission Mössbauer measurements were performed in transmission mode with a ^{57}Co radioactive source in constant acceleration mode using a standard PC based Mössbauer spectrometer equipped with a Weissel velocity drive. Velocity calibration of the spectrometer was done with a natural iron absorber at room temperature. High magnetic field ^{57}Fe Mössbauer measurements were carried out using a Janis superconducting magnet. For the high magnetic field measurements, the external field was applied parallel to the γ-rays (i.e., longitudinal geometry). Absorbers were carefully prepared to optimize both a good compactness and an adequate heat transmission. Analysis of the spectra was performed using the NORMOS least-squares fitting programs [37]. Doublets and sextets of Lorentzian lines were used, doublets in the paramagnetic region and sextets in the magnetic region respectively. The spectra were calibrated referring to α-Fe.

3 Results and discussion

The XRD patterns have been collected on the surfaces of the disks with a Rigaku diffractometer using Cu Kα radiation. Figure 1 shows the representative 2θ scans of XRD for the parent and Ti^{4+} as cation substituted α-$Fe_{2-x}Ti_xO_3$ (x = 0.0, 0.0206 and 0.0344) hematite. On comparing the observed spectra with the standard diffraction pattern (JCPDS file No. 86-0550), all Bragg peaks of the XRD patterns for the synthesized hematite in the doping range ($0.0 \leqslant x \leqslant 0.0344$) are assigned to α-Fe_2O_3 phase, and no other phase is identified. The XRD patterns for the α-$Fe_{2-x}Ti_xO_3$ are indexed as that of corundum type (α-Al_2O_3) structure at room temperature consistent with the earlier report [38].

The Raman spectra of the Ti^{4+} doped α-$Fe_{2-x}Ti_xO_3$ (x = 0.0, 0.0206 and 0.0344) hematite in the range of 100 cm^{-1} to 800 cm^{-1} at room temperature and normal pressure are illustrated in Fig. 2. The Raman spectra of parent α-Fe_2O_3, $Fe_{1.9794}Ti_{0.0206}O_3$ and $Fe_{1.9656}Ti_{0.0344}O_3$ with seven phonon modes (two A_{1g} modes, five E_g modes and one Raman inactive or disorder E_u mode) predicted from the group theory (Table 1) confirm the corundum structure. For hematite α-Fe_2O_3, the phonon

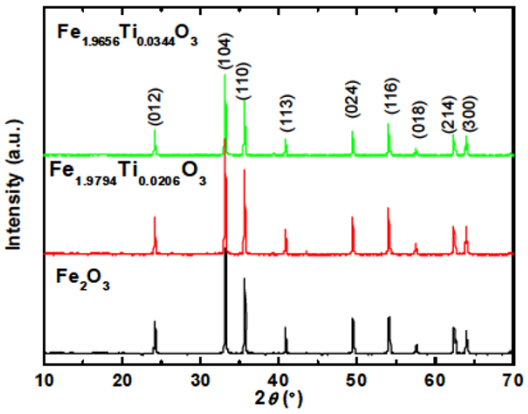

Fig. 1 XRD patterns for α-$Fe_{2-x}Ti_xO_3$ (x = 0.0, 0.0206 and 0.0344).

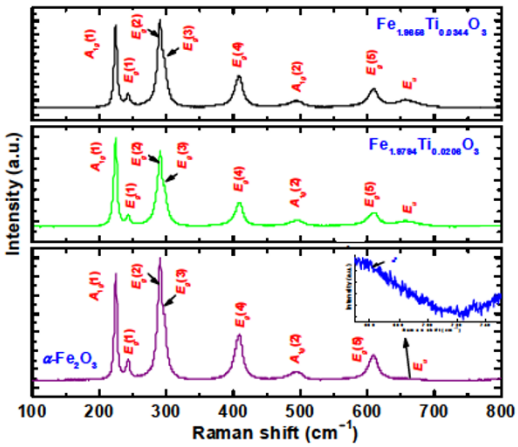

Fig. 2 Raman scattering intensities shown as a function of Raman shift (or wave number) for α-$Fe_{2-x}Ti_xO_3$ (x = 0.0, 0.0206 and 0.0344) at 300 K. Inset showing the E_u mode for α-Fe_2O_3.

Table 1 Raman shift (ν) and full width at half maximum (FWHM, Γ) for hematite at a laser power of 5 mW

Active mode	α-Fe_2O_3		$Fe_{1.9794}Ti_{0.0206}O_3$		$Fe_{1.9656}Ti_{0.0344}O_3$	
	ν (cm^{-1})	Γ (cm^{-1})	ν (cm^{-1})	Γ (cm^{-1})	ν (cm^{-1})	Γ (cm^{-1})
$A_{1g}(1)$	225	5.6	226	5.7	226	5.8
$E_g(1)$	244	6.8	245	6.9	245	6.9
$E_g(2)$	292	7.6	292	7.6	292	7.7
$E_g(3)$	298	7.9	296	7.9	—	—
$E_g(4)$	410	13.1	411	13.6	411	13.7
$A_{1g}(2)$	496	20.6	497	20.8	497	21.0
$E_g(5)$	611	14.1	612	14.4	612	14.3
E_u (disorder)	660	—	659	18.6	658	20.6

modes predicted by group theory are observed at $A_{1g}(1) \approx 225$ cm^{-1}, $E_g(1) \approx 244$ cm^{-1}, $E_g(2) \approx 292$ cm^{-1}, $E_g(3) \approx 298$ cm^{-1}, $E_g(4) \approx 410$ cm^{-1}, $A_{1g}(2) \approx 496$ cm^{-1}, and $E_g(5) \approx 611$ cm^{-1}, consistent with the reported values in the literature [8,9]. It is noticed that the Raman spectrum in the range of 620–750 cm^{-1} shows an additional feature, illustrating the Raman inactive and IR active E_u (LO) mode at about 660 cm^{-1} (the inset of Fig. 2).

On substitution of Ti at Fe site, all seven phonon modes are observed, and a small shift to higher wave numbers or Raman shift is seen in Fig. 2. The IR active E_u (LO) mode (≈ 660 cm^{-1} for hematite α-Fe_2O_3) becomes sharp on Ti substitution and the FWHM increases on enhancing the doping concentration. We note that IR active E_u (LO) mode at 659 cm^{-1} is not allowed in Raman spectra by group theory. The sharp feature of E_u (LO) mode occurs for Ti substitution in hematite α-Fe_2O_3 at about 660 cm^{-1} mode is attributed to the possible disorder induced by Ti surface defects or stress. The E_u mode of parent hematite is 660 cm^{-1} and decreases as a function of Ti doping, and it reaches at about 658 cm^{-1} for $x = 0.0344$. On the other hand, the FWHM increases from 6 cm^{-1} to 20 cm^{-1} consistent with the earlier measurements [10].

The increase in FWHM (i.e., bandwidth, as shown in Table 1) might also arises from local heating due to the relatively high laser power (≈ 5 mW), which enhances anharmonic interactions. In the present study, the laser power fixed to 5 mW (for all the samples) causes the bands to broaden and undergo a small shift to higher wave numbers or Raman shift, as illustrated in Table 1. Beattie and Gibson [9] argued that in α-Fe_2O_3 the bandwidth decreases and Fe band positions shift slightly to higher wave numbers at low temperature (77 K). This behavior seems to be fully reversible, as turning down the laser power causes the bandwidth to decrease.

We may refer to the work of McCarty and Boehme [11] who observed an additional band when chromium is substituted for iron in α-Fe_2O_3. The band ranges in Raman shift from 664 cm^{-1} for $Fe_{1.73}Cr_{0.27}O_3$ to 685 cm^{-1} for $Fe_{0.4}Cr_{1.6}O_3$, with the shift increasing nearly linearly with increasing Cr content. The present Raman spectra change gradually for Ti doping in α-$Fe_{2-x}Ti_xO_3$ ($x = 0.0$, 0.0206 and 0.0344), attributed to the strong electron–phonon interaction in this system. The $E_g(3)$ mode is more pronounced for lower doping ($x = 0.0206$), but for higher doping ($x = 0.0344$) it is not documented in the Raman spectra attributed to the fact that the non-magnetic ion Ti doping leads to structural changes in α-$Fe_{2-x}Ti_xO_3$ system. The FWHM increases as Ti doping increases (Table 1), consistent with earlier reported data [10,11].

Magnetic hysteresis measurements for Ti doped bulk hematite α-$Fe_{2-x}Ti_xO_3$ ($x = 0.0$, 0.0206 and 0.0344) were carried out in an applied magnetic field (H) at room temperature (300 K) as represented in Figs. 3–5. The hysteresis loop of the Ti doped α-Fe_2O_3 shows a ferromagnetic behavior for all the prepared samples. Moreover, the magnetization measurements of parent and Ti doped bulk hematite α-$Fe_{2-x}Ti_xO_3$ ($x = 0.0206$ and 0.0344) exhibit hysteretic features with coercivity being determined to be 995 Oe, 1404 Oe and 2023 Oe, respectively (Figs. 3–5). The remanence of all samples decreases as x increases. The observed value of remanence could be understood from the effect of competition between inter-particle interactions and intra-particle anisotropy on the spin relaxation process, which produces frustration. Coercivity is an extrinsic property of a magnet, which depends not only on the spin carrier but also on the shape or the size of the magnet [37]. The larger coercivity for Ti doped sample can be attributed to its enhanced shape and magneto-crystalline anisotropy. The parent α-Fe_2O_3 as well as Ti doped α-$Fe_{2-x}Ti_xO_3$ ($x = 0.0206$ and 0.0344) show the magnetic hysteresis loop at 300 K. We failed to observe saturation of the magnetization even under the

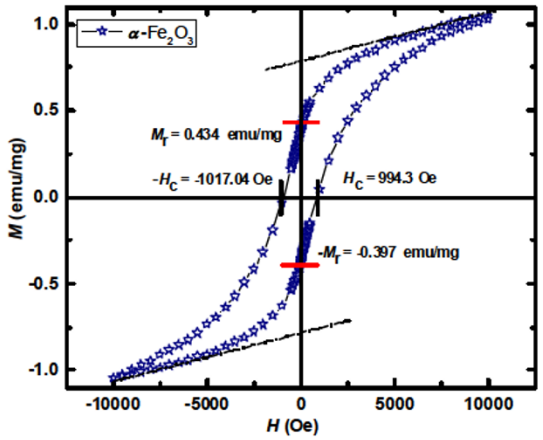

Fig. 3 Hysteresis loop for parent α-Fe_2O_3 sample at room temperature (300 K).

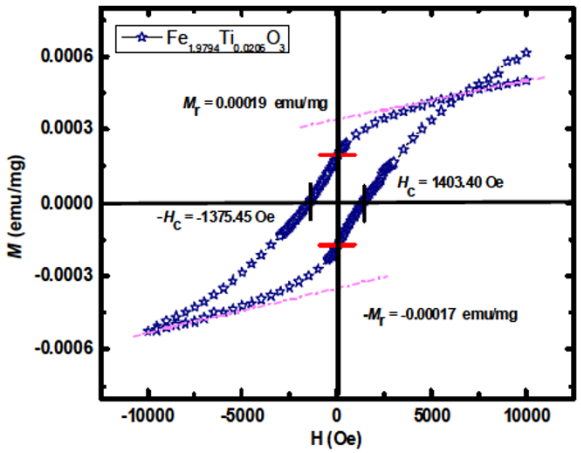

Fig. 4 Hysteresis loop for Ti doped hematite α-$Fe_{1.9794}Ti_{0.0206}O_3$ sample at room temperature (300 K).

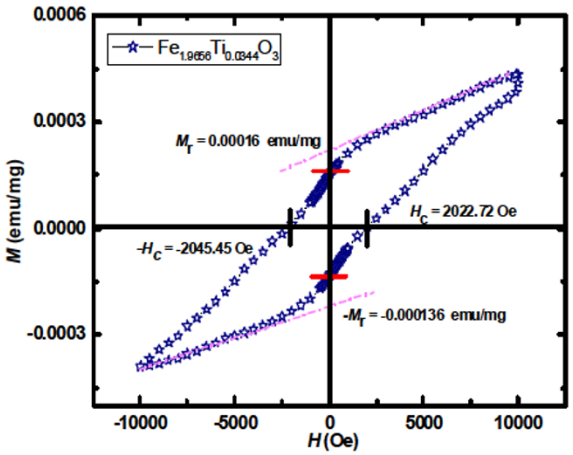

Fig. 5 Hysteresis loop for Ti doped hematite α-$Fe_{1.9656}Ti_{0.0344}O_3$ sample at room temperature (300 K).

maximum applied magnetic field 10 kOe for all samples (Figs. 3–5), while α-$Fe_{1.9794}Ti_{0.0206}O_3$ shows a butterfly loop which is not understood. These results are summarized in Table 2.

Table 2 Remnant magnetization (M_r) and coercive force (H_c) for Ti doped α-$Fe_{2-x}Ti_xO_3$

Sample	Remnant magnetization, M_r (emu/mg)	Coercive force, H_c (Oe)
α-Fe_2O_3	0.434	994.3
α-$Fe_{1.9794}Ti_{0.0206}O_3$	0.00019	1403.4
α-$Fe_{1.9656}Ti_{0.0344}O_3$	0.00016	2022.72

Hill and workers [16] observed the magnetic properties of bulk and mesoporous hematite α-Fe_2O_3 at room temperature as well as at low temperature. For bulk α-Fe_2O_3, no hysteresis loop is observed at 12 K, in line with what is expected for a simple antiferromagnet. At 295 K, hysteresis is observed due to the weak ferromagnetic state of the material. Extrapolation of the high-field region of the $M(H)$ curve (where saturation occurs) provides a spontaneous magnetization, M_r of 0.28 emu/mg. At room temperature, however, the bulk material is a harder magnet than the mesoporous material, H_c = ~0.17 T. These results are higher in magnitude as compared to our results for parent α-Fe_2O_3, which may be due to the morphological difference. He *et al.* [18] observed the effect of Co coated hematite, and he found that the magnetic properties are changed with Co coating. The coercivity of Co coated hematite is higher than that of pure hematite by about 400 Oe. In the present study of magnetization, the hysteretic features are changed gradually with Ti doping in α-$Fe_{2-x}Ti_xO_3$ (x = 0.0, 0.0206 and 0.0344), attributed to that magnetic properties are sensitive with doping concentration. It is well known that the magnetization of ferromagnetic materials is very sensitive to the morphology and structure of the as-synthesized sample, so the higher coercivity and lower remanent magnetization may be attributed to the shape anisotropy of α-$Fe_{2-x}Ti_xO_3$ superstructures, which prevent them from magnetizing in directions except their easy magnetic axes, hence leading to the higher coercivity.

The ^{57}Fe Mössbauer spectra recorded at 300 K for Ti doped α-$Fe_{2-x}Ti_xO_3$ (x = 0.0, 0.0206 and 0.0344) are illustrated in Fig. 6. The Mössbauer spectra are analyzed by considering single symmetric Lorentzian shaped sextet model for parent and doped hematite. The room temperature Mössbauer spectra are fitted with NORMOS-SITE program [37] and all samples show strong magnetic ordering. The obtained value of chi-2 is minimum, and NORMOS-SITE program is well fitted to the experimental data. The ^{57}Fe fitted Mössbauer parameters at room temperature are listed in Table 3. The Mössbauer parameters derived from the

Table 3 ^{57}Fe Mössbauer parameters for Ti doped α-$Fe_{2-X}Ti_XO_3$

Sample	Assignment	δ (mm/s)	ΔE_Q (mm/s)	B_{hf} (T)	Relative area (%)
α-Fe_2O_3	Sextet	0.38	0.43	51.8	100.00
α-$Fe_{1.9794}Ti_{0.0206}O_3$	Sextet	0.32	–0.19	52.0	100.00
α-$Fe_{1.9656}Ti_{0.0344}O_3$	Sextet	0.27	–0.21	50.9	76.84
	Doublet	0.23	0.37	0	23.16

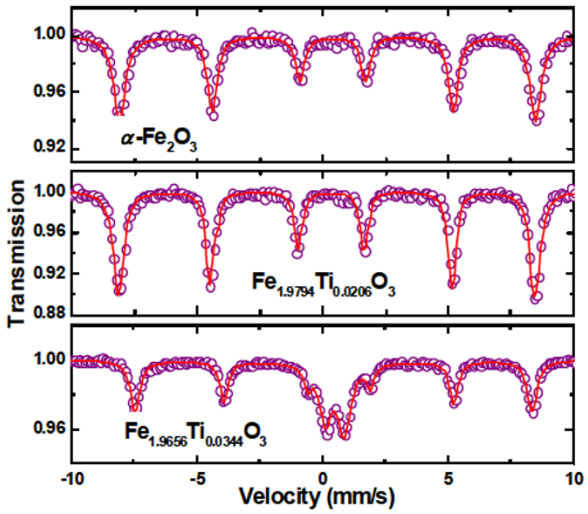

Fig. 6 Room temperature Mössbauer spectra for α-$Fe_{2-x}Ti_xO_3$ (x = 0.0, 0.0206 and 0.0344) hematite.

spectra using single symmetric Lorentzian shaped sextet model and an additional quadruple model are required for Ti doping (x = 0.0344). The obtained hyperfine parameters are with respect to natural iron, consistent with the earlier experimental data [21–27].

From Fig. 6, the transmission Mössbauer spectroscopy of α-Fe_2O_3 reveals only single sextet indicating magnetically ordered state. The peaks with high hyperfine field values are related to the irons involved in the electron delocalization process, without the presence of Ti as nearest neighbors. The transmission Mössbauer spectroscopy of α-$Fe_{1.9656}Ti_{0.0344}O_3$ shows an additional peak corresponding to those iron atoms surrounded by Ti neighbors as depicted in Fig. 6. The additional feature is more pronounced for Ti doping at x = 0.0344. It is noticed that the Fe site distributions become broader and occupy more area as the amount of Ti increases and the relative area decreases. The observed isomer shift δ from room temperature Mössbauer data clearly shows the presence of ferric (Fe^{3+}) and Ti^{4+} ions. The negative values of the quadruple coupling constants for all Ti doped hematite indicate that the material is weakly ferromagnetic at room temperature (Table 3). This is mainly because that the occupation by Ti^{4+} ions of interstitial sites replaces the vacancies on Fe^{3+} sites.

The room temperature Mössbauer spectra of α-$Fe_{1.9656}Ti_{0.0344}O_3$ hematite show an additional presence of a quadruple-split doublet [19,24–27]. The ^{57}Fe Mössbauer spectra of α-$Fe_{1.9656}Ti_{0.0344}O_3$ recorded at 300 K show clear sextet pattern and a broad doublet. The doublet component values of isomer shift δ is 0.23 mm/s and quadrupole ΔE_Q is 0.37 mm/s at 300 K. The NORMOS-SITE program fitting for Mössbauer spectra of the magnetically split component of α-$Fe_{1.9656}Ti_{0.0344}O_3$ to a single sextet yields a hyperfine magnetic field (B_{hf} of 51.0±0.3 T) smaller as compared to that of pure α-Fe_2O_3 (B_{hf} of 51.8±0.3 T).

Furthermore, the line width of α-$Fe_{1.9656}Ti_{0.0344}O_3$ 0.23 mm/s is an indicative of a distribution of sites originating from the presence of the dopant Ti^{4+} within the α-Fe_2O_3 structure. The spectra are therefore fitted with sextet pattern, and the field values (B_{hf}) are smaller for all Ti doped hematite α-$Fe_{2-x}Ti_xO_3$. The above features indicate that α-$Fe_{1.9656}Ti_{0.0344}O_3$ is weakly ferromagnetic at room temperature as compared to the parent α-Fe_2O_3. In the α-Fe_2O_3 pattern, the larger field (B_{hf} = 51.8±0.3 T) can be associated with Fe^{3+} ions which are not influenced by the presence of Ti, while in α-$Fe_{1.9656}Ti_{0.0344}O_3$ the smaller field (B_{hf} = 51.0±0.3 T) can be assigned to Fe^{3+} ions that have Ti^{4+} ions in close proximity. The relative population of each magnetic component varied with assumed linewidth without any significant change to the value of χ^2 and the percentage of Fe^{3+} influenced by Ti is therefore difficult to quantify.

4 Conclusions

The structural and magnetic ordering effects in polycrystalline α-$Fe_{2-x}Ti_xO_3$ (x = 0.0, 0.0206 and 0.0344) are studied by XRD, Raman and Mössbauer spectroscopy. The crystal structure of the samples is studied using XRD. The XRD patterns identify the single phase and corundum (Al_2O_3) type structure of all the polycrystalline samples.

The Raman spectra reveal seven Raman active modes (two A_{1g} modes and five E_g modes) and an

additional Raman inactive E_u mode. The IR active E_u (LO) mode ($\approx 660\ cm^{-1}$ for hematite α-Fe_2O_3) becomes sharp on Ti substitution and the FWHM increases on enhancing the doping concentration. The $E_g(3)$ mode is more pronounced for lower doping ($x = 0.0206$), but for higher doping ($x = 0.0344$) is not documented in the Raman spectra attributed to the fact that the non-magnetic Ti ion doping leads to structural changes in α-$Fe_{2-x}Ti_xO_3$ system. The FWHM increases as Ti doping increases. Increase in Γ with Ti doping concentration is attributed to enhanced α-Fe_2O_3 bandwidth due to presence of Ti ion in the lattice as well as local heating by the relatively high laser power, which enhances anharmonic interactions.

The coercivity of Ti doped hematite increases as x increases, while the remanence decreases as x increases. The coercivity H_c (remanence M_r) for $x = 0.0$, 0.0206 and 0.0344 are determined to be 995 Oe (0.44 emu/mg), 1404 Oe (0.00019 emu/mg) and 2023 Oe (0.00016 emu/mg), respectively. The larger coercivity for Ti doped sample can be attributed to its enhanced shape and magneto-crystalline anisotropy. The room temperature ^{57}Fe transmission Mössbauer spectroscopy of α-Fe_2O_3 reveals only single sextet indicating magnetically ordered state; however, a quadruple-split doublet is used for doped α-$Fe_{2-x}Ti_xO_3$ ($x = 0.0$, 0.0206 and 0.0344) implying weak magnetic ordering. The observed isomer shift δ from room temperature Mössbauer data clearly shows the presence of ferric (Fe^{3+}) and Ti^{4+} ions, illustrating strong ferromagnetic ordering up to $x = 0.0206$ in α-$Fe_{2-x}Ti_xO_3$ hematite and weak ferromagnetic ordering for α-$Fe_{1.9656}Ti_{0.0344}O_3$ hematite.

Acknowledgements

Authors are thankful to UGC-DAE CSR, Indore for providing characterization facilities.

References

[1] Saragovi C, Arpe J, Sileo E, *et al*. Changes in the structural and magnetic properties of Ni-substituted hematite prepared from metal oxinates. *Phys Chem Miner* 2004, **31**: 625–632.

[2] Van Van San E, De Grave E, Vandenberghe RE, *et al*. Study of Al-substituted hematites, prepared from thermal treatment of lepidocrocite. *Phys Chem Miner* 2001, **28**: 488–497.

[3] Zysler RD, Fiorani D, Testa AM, *et al*. Size dependence of the spin-flop transition in hematite nanoparticles. *Phys Rev B* 2003, **68**: 212408.

[4] Dang M-Z, Rancourt DG, Dutrizac JE, *et al*. Interplay of surface conditions, particle size, stoichiometry, cell parameters, and magnetism in synthetic hematite-like materials. *Hyperfine Interact* 1998, **117**: 271–319.

[5] Bruzzone CL, Ingalls R. Mössbauer-effect study of the Morin transition and atomic positions in hematite under pressure. *Phys Rev B* 1983, **28**: 2430.

[6] Hofmann M, Campbell SJ, Kaczmarek WA, *et al*. Mechanochemical transformation of α-Fe_2O_3 to $Fe_{3-x}O_4$—Microstructural investigation. *J Alloys Compd* 2003, **348**: 278–284.

[7] Bersani D, Lottici PP, Montenero A. Micro-Raman investigation of iron oxide films and powders produced by sol–gel syntheses. *J Raman Spectrosc* 1999, **30**: 355–360.

[8] Shim S-H, Duffy TS. Raman spectroscopy of Fe_2O_3 to 62 GPa. *Am Mineral* 2001, **87**: 318–326.

[9] Beattie IR, Gibson TR. The single-crystal Raman spectra of nearly opaque materials. Iron (III) oxide and chromium (III) oxide. *J Chem Soc A* 1970: 980–986.

[10] McCarty KF. Inelastic light scattering in α-Fe_2O_3: Phonon vs magnon scattering. *Solid State Commun* 1988, **68**: 799–802.

[11] McCarty KF, Boehme DR. A Raman study of the systems $Fe_{3-x}Cr_xO_4$ and $Fe_{2-x}Cr_xO_3$. *J Solid State Chem* 1989, **79**: 19–27.

[12] Zhao Y, Dunnill CW, Zhu Y, *et al*. Low-temperature magnetic properties of hematite nanorods. *Chem Mater* 2007, **19**: 916–921.

[13] Bødker F, Hansen MF, Koch CB, *et al*. Magnetic properties of hematite nanoparticles. *Phys Rev B* 2000, **61**: 6826.

[14] Rath C, Sahu KK, Kulkarmi SD, *et al*. Microstructure-dependent coercivity in monodispersed hematite particles. *Appl Phys Lett* 1999, **75**: 4171.

[15] Gregg KA, Perera SC, Lawes G, *et al*. Controlled synthesis of MnP nanorods: Effect of shape anisotropy on magnetization. *Chem Mater* 2006, **18**: 879–886.

[16] Hill AH, Jiao F, Bruce PG, *et al*. Neutron diffraction study of mesoporous and bulk hematite, α-Fe_2O_3.

Chem Mater 2008, **20**: 4891–4899.

[17] Ayub I, Berry FJ, Bilsborrow RL, *et al*. Influence of zinc doping on the structural and magnetic properties of α-Fe_2O_3. *J Solid State Chem* 2001, **156**: 408–414.

[18] He T, Luo H-L, Li S. Effect of cobalt on the morin transition of hematite. *J Magn Magn Mater* 1988, **71**: 323–328.

[19] Barrero CA, Arpe J, Sileo E, *et al*. Ni- and Zn-doped hematite obtained by combustion of mixed metal oxinates. *Physica B* 2004, **354**: 27–34.

[20] Morrish AH. *Canted Antiferromagnetism*: *Hematite*. Singapore: World Scientific Publishing Company, 1994.

[21] Stewart SJ, Borzi RA, Cabanillas ED, *et al*. Effects of milling-induced disorder on the lattice parameters and magnetic properties of hematite. *J Magn Magn Mater* 2003, **260**: 447–454.

[22] Sileo EE, Daroca DP, Barrero CA, *et al*. Influence of the genesis on the structural and hyperfine properties of Cr-substituted hematites. *Chem Geol* 2007, **238**: 84–93.

[23] Ericsson T, Krisnhamurthy A, Srivastava BK. Morin-transition in Ti-substituted hematite: A Mössbauer study. *Phys Scr* 1986, **33**: 88.

[24] Yogi A, Varshney D. Cu doping effect of hematite (α-$Fe_{2-x}Cu_xO_3$): Effect on the structural and magnetic properties. *Mat Sci Semicon Proc* 2014, **21**: 38–44.

[25] Yogi A, Varshney D. Magnetic and structural properties of pure and Cr-doped hematite: α-$Fe_{2-x}Cr_xO_3$ ($0 \leqslant x \leqslant 1$). *J Adv Ceram* 2013, **2**: 360–369.

[26] Varshney D, Yogi A. Influence of Cr and Mn substitution on the structural and spectroscopic properties of doped hematite: α-$Fe_{2-x}M_xO_3$ ($0.0 < x < 0.50$). *J Mol Struct* 2013 **1052**: 105–111.

[27] Varshney D, Yogi A. Structural, electrical and magnetoresistance of titanium-doped iron (II,III) oxide (Fe_3O_4) thin films deposited on strontium titanate, alumina, silicon, and float glass. *Mat Sci Semicon Proc* 2014, **26**: 33–40.

[28] Varshney D, Yogi A. Structural and transport properties of stoichiometric and Cu^{2+}-doped magnetite: $Fe_{3-x}Cu_xO_4$. *Mater Chem Phys* 2010, **123**: 434–438.

[29] Varshney D, Yogi A. Structural and electrical conductivity of Mn doped hematite (α-Fe_2O_3) phase. *J Mol Struct* 2011, **995**: 157–162.

[30] Varshney D, Yogi A. Structural and transport properties of stoichiometric Mn^{2+}-doped magnetite: $Fe_{3-x}Mn_xO_4$. *Mater Chem Phys* 2011, **128**: 489–494.

[31] Jiang Z, Liu Q, Barrón V, *et al*. Magnetic discrimination between Al-substituted hematites synthesized by hydrothermal and thermal dehydration methods and its geological significance. *J Geophys Res*: *Sol Ea* 2012, **117**, DOI: 10.1029/2011JB008605.

[32] Jiang Z, Rochette P, Liu Q, *et al*. Pressure demagnetization of synthetic Al substituted hematite and its implications for planetary studies. *Phys Earth Planet In* 2013, **224**: 1–10.

[33] Lee MH, Park JH, Han HS, *et al*. Nanostructured Ti-doped hematite (α-Fe_2O_3) photoanodes for efficient photoelectrochemical water oxidation. *Int J Hydrogen Energ* 2013, DOI: 10.1016/j.ijhydene.2013.10.031.

[34] Kumari S, Singh AP, Sonal, *et al*. Spray pyrolytically deposited nanoporous Ti^{4+} doped hematite thin films for efficient photo electrochemical splitting of water. *Int J Hydrogen Energ* 2010, **35**: 3985–3990.

[35] Lian X, Yang X, Liu S, *et al*. Enhanced photoelectron-chemical performance of Ti-doped hematite thin films prepared by the sol–gel method. *Appl Surf Sci* 2012, **258**: 2307–2311.

[36] Kleiman-Shwarsctein A, Hu Y-S, Stucky GD, *et al*. NiFe-oxide electrocatalysts for the oxygen evolution reaction on Ti doped hematite photoelectrodes. *Electrochem Commun* 2009, **11**: 1150–1153.

[37] Ruebenbauer K, Birchall T. A computer programme for the evaluation of Mössbauer data. *Hyperfine Interact* 1979, **7**: 125–133.

[38] Li L, Chu Y, Liu Y. Synthesis and characterization of ring-like α-Fe_2O_3. *Nanotechnology* 2007, **18**: 105603.